UV-curing assisted direct ink writing of dense, crack-free and high-performance zirconia-based composites with aligned alumina platelets

Maoyin Li[1,2], Shuigen Huang[1], Evita Willems[1], Jeroen Soete[1], Masanao Inokoshi[3], Bart Van Meerbeek[2], Jef Vleugels[1], Fei Zhang[1,2*]

[1] KU Leuven, Department of Materials Engineering, Kasteelpark Arenberg 44, B-3001 Leuven, Belgium.

[2] KU Leuven, Department of Oral Health Sciences, BIOMAT - Biomaterials Research group & UZ Leuven (University Hospitals Leuven), Dentistry, Kapucijnenvoer 7 block a, B-3000 Leuven, Belgium.

[3] Department of Gerodontology and Oral Rehabilitation, Graduate School of Medical and Dental Sciences, Tokyo Medical and Dental University, 1-5-45 Yushima, Bunkyo, Tokyo, 113-8549, Japan.

Abstract

Additive manufacturing (AM) of high-performance structural ceramic components with comparative strength and toughness as conventionally manufactured ceramics remains challenging. Here, an UV-curing approach is integrated in direct ink writing (DIW), taking advantage from DIW to enable an easy use of high solid-loading pastes and multi-layered materials with compositional changes, while avoiding drying problems. UV-curable opaque zirconia-based slurries with a solid loading of 51 vol% were developed to fabricate dense and crack-free alumina-toughened zirconia (ATZ) containing 3 wt% alumina platelets. Importantly, a non-reactive diluent was added to relieve polymerization-induced internal stresses, avoid subsequent warping and cracking, and facilitate the de-binding. For the first time, UV-curing

assisted DIW-printed ceramic after sintering revealed even better mechanical properties than that processed by a conventional pressing. This was attributed to the aligned alumina platelets, enhancing crack deflection and improving the fracture toughness from 6.8 ± 0.3 MPa $m^{0.5}$ (compacted) to 7.4 ± 0.3 MPa $m^{0.5}$ (DIW). The 4-point bending strength of the DIW ATZ (1009 ± 93 MPa) was also higher than that of the conventionally manufactured equivalent (861 ± 68 MPa). Beside homogeneous ceramic, laminate structures were demonstrated. This work has provided a valuable hybrid approach to additively manufacture tough and strong ceramic components.

Keywords: Direct ink writing; DIW; UV-curing; Zirconia ceramics; Non-reactive diluent; Platelet; Platelet alignment; Laminate structures.

1 Introduction

Additive manufacturing (AM) offers a mold-free route to counter the typical geometrical restrictions of traditional ceramic manufacturing processes and enables geometrical and functional complexity [1]. Although AM has widely been demonstrated to enable the production of various porous ceramic components, the fabrication of dense, crack-free and mechanically strong ceramic components without post-processing steps like infiltration and isostatic pressing remains a challenge. This is also an important reason why the implementation of AM technology in the ceramic industry has been slower than in the polymer and metal industry [1,2]. A number of slurry-based AM processes have been and continue to be investigated to fabricate dense and strong ceramic components, among which extrusion-based direct ink writing (DIW) is an important one [1,3].

DIW, also known as robocasting, allows building objects with controlled architecture and composition by continuous paste or discontinuous droplet-ink extrusion through a nozzle [4,5]. DIW can easily enable larger layer thicknesses and high-solid loading (>50 vol%) of viscous pastes to print 3D parts with high green density [6–8]. Powder loads below 40 vol%, on the other hand, are normally applied in vat polymerization/stereolithography (SLA) and inject printing slurries for good flowability and spreadability[9–13]. Although SLA ceramic slurries can reach a high solid loading > 50 vol% [14,15], the rheological requirements to control the viscosity in SLA to ensure a good flowability are in general higher than for DIW. Moreover, DIW opens up unlimited opportunities for processing multi-materials by using multiple printheads or combined material printheads [16].

According to different hardening principles, various ceramic slurries/pastes have been developed for DIW [17–19]. One type is solvent-based and relies on solvent evaporation, for which various aqueous/non-aqueous systems have been developed [20,21]. For non-aqueous systems, quick solvent evaporation may cause clogging during printing with fine nozzles and crack formation after printing, this along with the possible toxicity problem of organic solvents. However, the evaporation rate of non-toxic aqueous solvents is slow, requiring prolonged drying. Another common choice of DIW paste is a gel-embedded suspension and the use of thermosensitive hydrogel, such as Pluronic F-127, has widely been reported [17,22,23]. Hydrogel-based paste that satisfies both flowability in the nozzle and relatively high yield strength to self-support the weight of additional layers usually has a narrow rheological property window [24,25]. The drying process needs to be slow as well in order to avoid crack formation. Alternatively, a photocurable ceramic paste, similar to the one for ceramic SLA, can be used for DIW to combine the specific advantages of DIW and SLA (see illustration of the hybrid printing process in Fig. S1). Using a hybrid DIW-UV curing process, high solid-loaded

viscous pastes can be extruded and instantaneously hardened by UV-irradiation induced polymerization, resulting in a higher packing density and excluding the issues of the drying process. Such a hybrid process that combines ceramic extrusion with photopolymerization has recently drawn interest to fabricate ceramic and metal objects [26–32]. DIW-printing of aluminum parts was also explored with a high solid loading of 60 vol%, however, a thermal curing was applied after UV-curing, due to the limited curing depth [32]. Manufacturing crack-free and mechanically strong objects by UV-curing assisted DIW was so far not possible. To make this possible, the photocurable slurry/paste used for SLA/DLP needs to be carefully adjusted for DIW. The layer thickness in DIW, typically 100-400 µm thick depending on the nozzle size, is much thicker than in SLA, typically exhibiting a 10-30 µm layer thickness. This larger DIW layer thickness reduces polymerization efficiency at the bottom of each layer due to the limited UV-light penetration depth [26]. The involved UV-light scattering by the contained ceramic particles also results in a polymerization gradient with a polymerization efficiency gradually reducing from the layer top to its bottom and even resulting in an under-cured soft body at the bottom of the printed filament. Such inhomogeneous polymerization might additionally induce uneven shrinkage, resulting in warping and delamination of the built object and inhibiting continuation of the building process.

In addition, the UV-curing reactivity of a ceramic paste is significantly influenced by different factors, including UV-light intensity, curing time, powder concentration, particle size and distribution, and the refractive index of the ceramic material. In particular, zirconia remains one of the challenging ceramics due to the relatively high refractive index (2.24 at 365 nm) [33]. AM of zirconia ceramics nevertheless has much potential for various structural and functional applications, such as to produce turbine-blade cores, photonic crystals for advanced millimeter wave applications, fuel cells, dental prostheses, etc, all involving

customized design of complex geometries and combining different materials [34,35]. In this study, alumina-toughened zirconia (ATZ), containing 20 wt% alumina (3 wt% platelets and 17 wt% particles) and 0.4 mol% La_2O_3-doped 2Y-TZP, was printed. This ATZ composition was formulated based on previous research [36], but with alumina platelets addition aiming to further improve crack resistance [37–39]. The platelet addition of 3 wt% was decided according to our pilot study showing that the addition of > 3 wt% alumina platelets resulted in inter-platelet bridging and a reduced sintered density (Fig. S2 in supplementary information). Here, we particularly explored the potential of platelet alignment by DIW. Due to the high aspect-ratio and the shear forces arising from extrusion, the platelets and/or fibers in the paste can be aligned parallel to the extrusion direction [40–42]. As benefit, improved crack resistance was reported for ceramic-polymer composites especially in light of bioinspired material architectures [43,44].

Hereby, we developed a photocurable ceramic paste for UV-assisted DIW with a powder load above 50 vol% to ensure high density after sintering. A non-reactive, low viscous and water-soluble diluent was added to the paste to relieve polymerization shrinkage-induced stresses and warping during printing and to avoid subsequent cracking and delamination during de-binding. This non-reactive diluent can partially be removed by immersion in water to create channels for gas evacuation during the thermal de-binding process. Alumina platelets were beneficially aligned during the nozzle-extrusion process. Combining all these factors, fully dense and crack-free ATZ ceramics could be processed by UV-curing assisted DIW, resulting in competitive or even better mechanical properties than that processed by a conventional pressing. The possibility to build crack-free and dense multi-layered objects with changes in the composition was demonstrated by alternating layers of platelet-containing and platelet-free ATZ composites.

2 Results and discussion

2.1 Paste development to reduce polymerization-induced internal stresses and eliminate printing defects

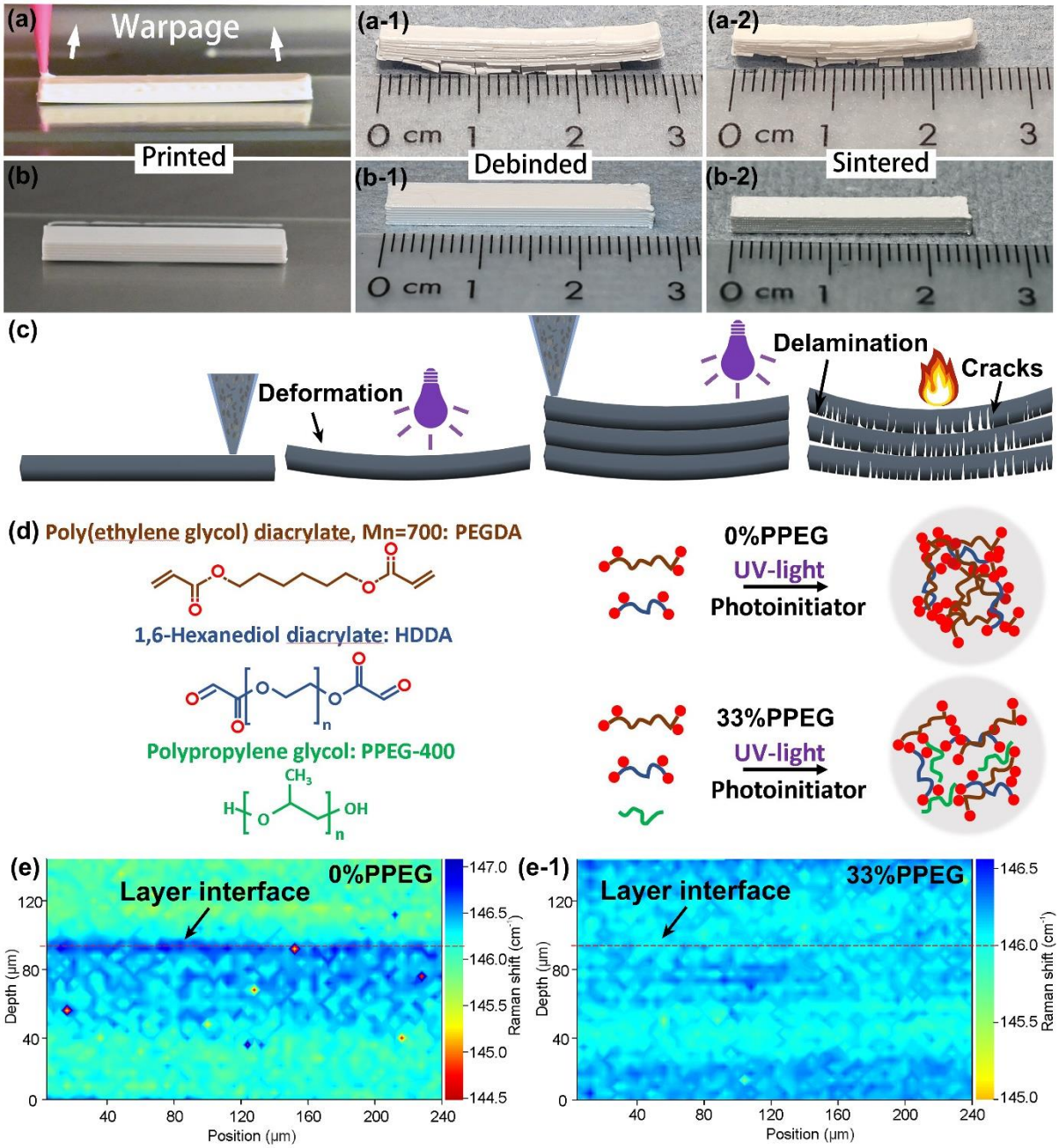

Fig. 1. Effect of non-reactive diluent on paste printability and the resultant ceramic quality: (a, a-1, a-2) Specimen without non-reactive diluent (0%PPEG), revealing internal stress-induced deformation, cracking and delamination; (b, b-1, b-2) Specimen with non-reactive diluent addition (33%PPEG), exhibiting no deformation and resulting in dense and crack-free samples; (c) Schematic of the internal stress caused by the polymerization volume shrinkage during UV-curing; (d) Mechanism of the non-reactive diluent addition decreased the internal stress by suppressing the cross-linking between monomers; (e) Stress distribution analyzed by micro-

Raman on cross-sections of printed and UV-cured 0%PPEG and (e-1) 33%PPEG (before de-binding and sintering).

As shown in Fig. 1a-b, the developed paste loaded with 51 vol% ATZ powder can successfully be printed using the hybrid DIW-UV curing process (see supplementary section Fig. S1). Although the packing density of printed ATZ was lower than that of the conventionally compacted specimen (Table 1), 51 vol% was high enough to fabricate dense ceramics after sintering. Crucial for this paste was the addition of the non-reactive diluent (PPEG-400) which avoided deformation of the printed objects as well as cracks and delamination in the de-binded and sintered objects. Without non-reactive diluent (0%PPEG, Fig. 1a), specimen warpage indicated that internal stresses were induced by polymerization accompanied by a volume shrinkage. The two monomer compounds, i.e. PEGDA (Mn700) and HDDA, were subjected to weak van der Waals forces and hydrogen bonding in their liquid state with an intermolecular distance of 0.3-0.5 nm, whereas polymerization converted the acrylate double bonds into strong and short covalent bonds with a length of ~0.154 nm. Therefore, a volume shrinkage of ~1-4% accompanied the polymerization [45–49]. Furthermore, light-scattering by the ceramic particles can result in a gradual decrease in monomer conversion and cross-linking density across the layer thickness [50,51]. And this was severer for zirconia as the refractive index of zirconia (2.24) is higher than that of most ceramics, i.e., alumina ~1.79, and of cured or uncured PEGDA (1.475 at a light wavelength of 365 nm) [49–53]. This polymerization gradient and polymerization-induced volumetric shrinkage, enhanced with increased number of printed layers, resulted in deformation and an uneven stress distribution within the printed object. De-binding and sintering subsequently gave rise to severe cracking and delamination at the most vulnerable interfaces between the printing layers of the AM part (Fig. 1c and Fig. S3).

Adding the non-reactive diluent (33%PPEG) to the paste reduced volumetric shrinkage during curing and the resultant polymerization-induced internal stresses (Fig. 1b). For polymerization reaction, the chains within the growing network need to be in close proximity, while the non-reactive diluent molecules partially separate the reactive sites of the monomers, as schematically presented by the green PPEG molecules separating the red colored functional groups on PEGDA and HDDA molecules in Fig. 1d. Cross-linking between monomers was hence suppressed, giving rise to a reduced volumetric shrinkage. The polymerization reaction was to support and keep the printed ceramic structure and fixate the alignment of the textured alumina platelets. The polymerized monomers are not maintained in the final ceramic product and are completely removed in the debinding and sintering steps. The mechanical strength of the polymer, the conversion degree of monomers as well as the interaction between the organic and ceramic phases are therefore not critical for the final product. The most important feature here is to avoid the excess stress that can cause warping and delamination during polymerization. The reduced polymerization-induced stresses (33%PPEG vs. 0%PPEG) were confirmed by micro-Raman stress analysis across the interface between the printed layers of cross-sectioned specimens (Fig. 1e and e-1). Stresses clearly concentrated at the interface between two printing layers of 0%PPEG, while they were homogenized upon diluent addition (33%PPEG). Decreased polymerization shrinkage and concomitant reduced stress production achieved by adding non-reactive diluent was in agreement with previous reports when water and poly(ethylene glycol) 200 (PEG-200) were added to the photopolymer slurry to print polyurethane-acrylic and ceramic composites by SLA [47,54,55].

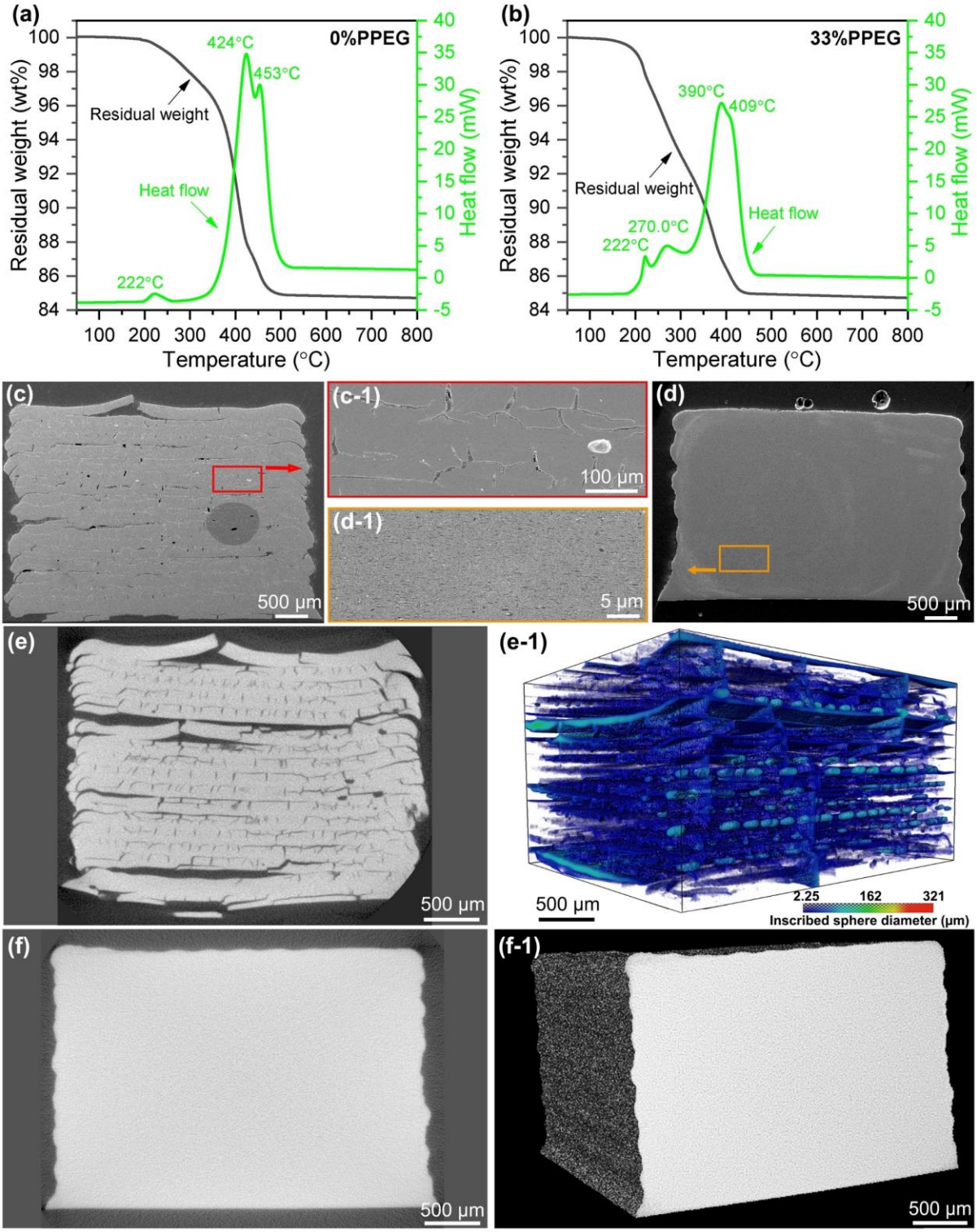

Fig. 2. (a) TGA/DSC of printed samples using slurries without non-reactive diluent (0%PPEG) and (b) with non-reactive diluent (33%PPEG); SEM morphology of polished ceramic cross-section of (c, c-1) 0%PPEG and (d, d-1) 33%PPEG after sintering; (e) representative XCT slice of sintered 0%PPEG and (e-1) 3D-reconstruction of defects detected in sintered 0%PPEG; (f) representative XCT slice and (f-1) bulk 3D-reconstruction view of sintered 33%PPEG.

In addition, adding non-reactive diluent PPEG-400 facilitated the de-binding, because PPEG-400 is water-soluble, hereby creating a network of pores within the sample. The formed porous network can prevent high gas-pressure built-up in the subsequent thermal polymer-decomposition process at higher temperature [47,56], and facilitate polymer-decomposition product removal during thermal de-binding. According to TGA/DSC analysis (Fig. 2a and b), heating between ~180°C to ~500°C removes the organic components. The weight loss of 0%PPEG started at 200°C and was completed at ~500°C with three heat flow peaks at 222°C, 424°C and 453°C, which corresponded to the discharge of BYK-111, the pyrolysis of cured HDDA and pyrolysis of cured PEGDA, respectively. In comparison, 33%PPEG objects had an extra DSC peak at 270°C, corresponding to the removal of the residual non-reactive diluent after water de-binding. The pyrolysis temperature for cured HDDA and PEGDA decreased from 424°C and 453°C to 390°C and 409°C, respectively. This beneficial effect should be attributed to the addition of non-reactive diluent, which suppressed cross-linking between monomers and resulted in shorter polymer production, reducing the pyrolysis temperature needed. Since the non-reactive diluent has a relatively low boiling point, as compared to the de-polymerization temperature of cured HDDA and PEGDA, removal of the non-reactive diluent (residual PPEG-400 after water de-binding) should additionally have formed an interconnected pore network that facilitates gas effusion from the specimens when cured HDDA and PEGDA are decomposed.

To this end, the non-reactive diluent addition was essential to relieve the polymerization-induced internal stresses and subsequently produce crack-free ceramics. Without non-reactive diluent, printed and sintered specimens were full of defects with especially large layer delamination (Fig. 2c, c-1 and Fig. 2e, e-1). As quantified from XCT results (Fig. S3), defects related to the delamination were extended to over 300 μm along the printing layers and voids

of 0-50 μm were penetrated into each layer. Thanks to the absence of stress concentrations between the printing layers and the easier de-binding process by adding non-reactive diluent, sintered 33%PPEG appeared dense and crack-free without defects and delamination that are often observed in AM ceramics, as was confirmed by SEM (Fig. 2d and d-1) and XCT (Fig. 2f and f-1). In addition, when increasing the powder loading to 53 vol%, the extruded filaments were too stiff without enough flowability, resulting in discontinuously distributed triangle-shaped defects with a size of 40-120 μm in-between the filaments, although large delamination defects remained avoided (Fig. S4). XRD also confirmed the absence of monoclinic ZrO_2 phase in crack-free ATZ (Fig. S5-33%PPEG after sintering).

2.2. AM of laminated structures

The multi-layered materials with changes in the composition were printed using two different ATZ compositions. Besides the studied ATZ composition with 3 wt% alumina platelets (3AP), another ATZ with the same overall composition (i.e., 20 wt% alumina toughened 2Y-TZP) but without alumina platelets (0AP) was used in the deposition of laminate structure. Two pastes with the same solid loading of 51 vol% were prepared and the ceramic laminates were built using two printheads to alternate the composition of each layer, as shown in Fig. 3a, or of every two layers, as shown in Fig. 3b. Scanning electron micrographs revealed layers with a clear boundary without inter-layer delamination or defects (Fig. 3b-1). However, due to the different sintering shrinkage rates between the two materials, the laminate object had to be designed and printed in a symmetrical structure to avoid bending during sintering. As shown in Fig. S6a, where half the object was composed of 3AP and another half of 0AP, sample warping was observed after sintering due to the fact that the sintering shrinkage of 0AP was slightly higher than that of 3AP. A sandwich configuration with 0AP surrounded by 3AP did not

warp after sintering (Fig. S6b). In addition, the alumina platelets in the 3AP layer are shown to be well aligned along the printing direction, which was further confirmed by the elemental mapping of the interface (Fig. 3c). The few elongated Al-containing particles that were not aligned also contained lanthanum, implying these randomly oriented elongated particles are lanthanum hexa-aluminate grains, in agreement with previous work [36]. In contrast to the alumina platelets that could be textured during printing, the lanthanum hexa-aluminate needles were formed in-situ during the sintering process and were therefore not aligned.

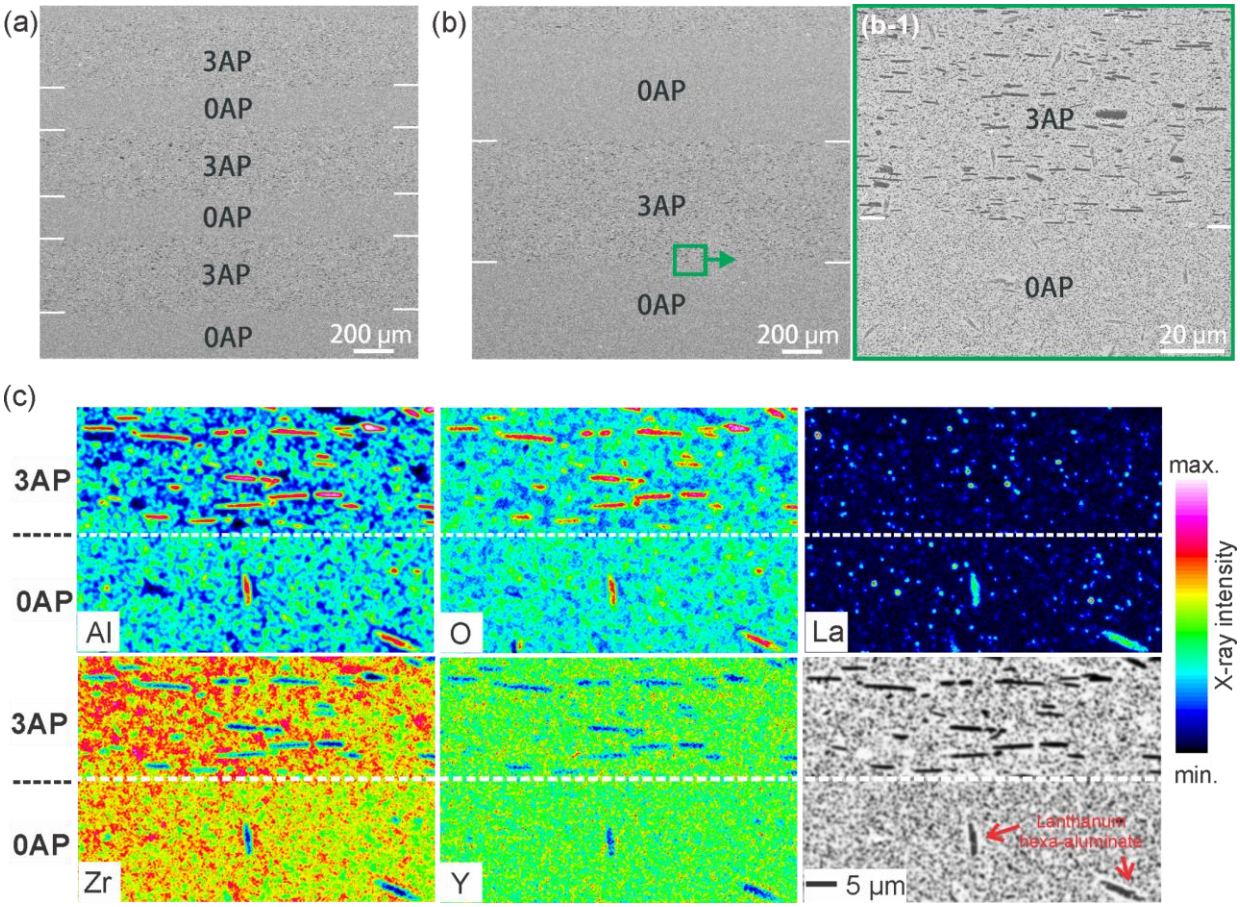

Fig. 3. Multi-layered laminate structure consisting of platelet-free (0AP) and 3 wt% platelet-containing (3AP) layers. The laminate was made by (a) alternating each printing layer, (b, b-1) alternating every two printing layers and (c) elemental map at the interface of 3AP and 0AP showing the alignment and distribution of alumina platelets.

2.3 Microstructure and mechanical properties of sintered objects

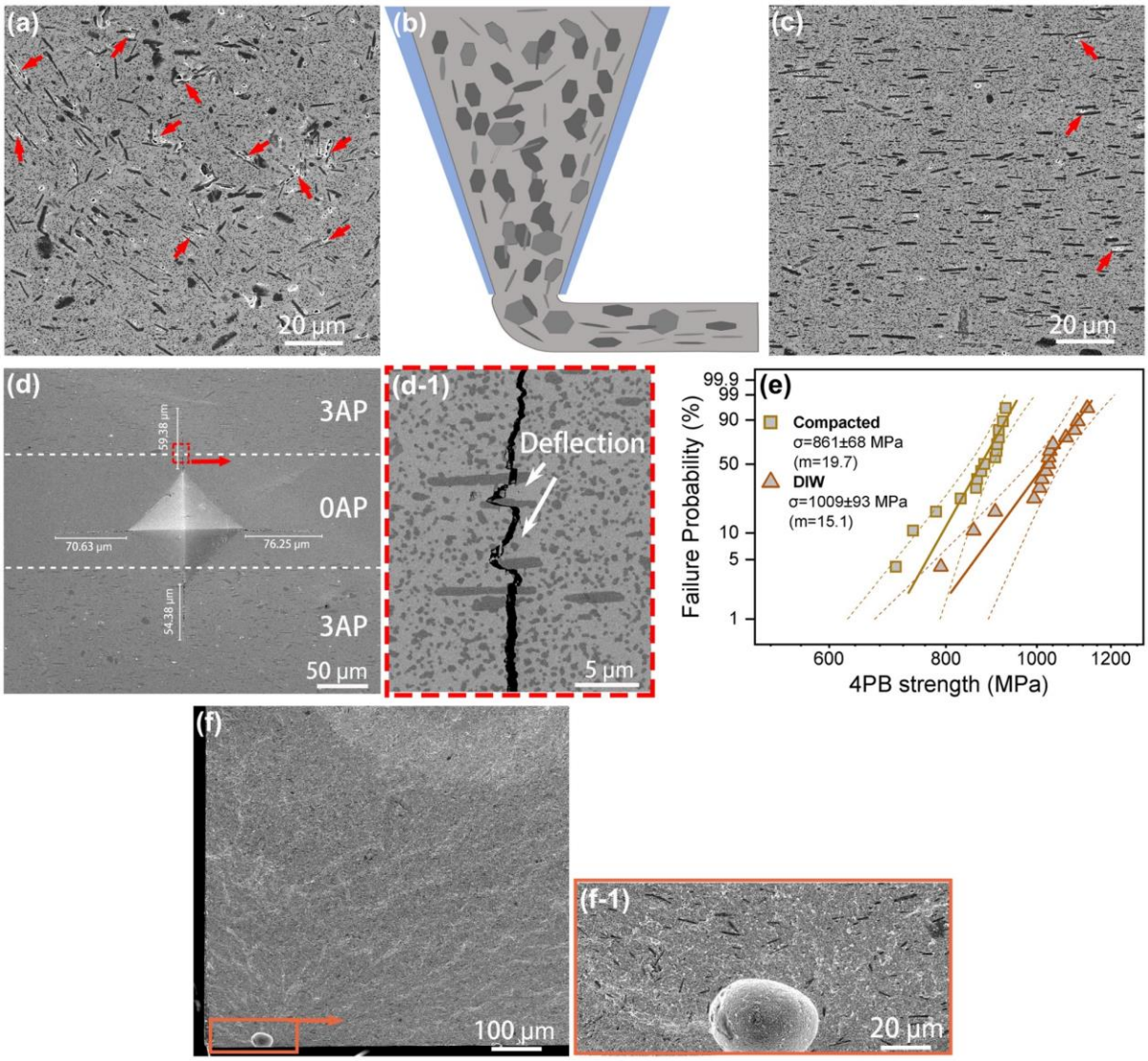

Fig. 4. Microstructure and mechanical property comparison of ATZ ceramics (3AP with 3 wt% alumina platelets) manufactured by conventional compacting and DIW. (a) Inter-platelet bridging caused pores in conventionally compacted ATZ ceramics; (b) Schematic of platelet alignment during the nozzle-extrusion process; (c) Microstructure of DIW-processed ceramics; (d, d-1) Crack deflection toughening by the aligned alumina platelets; (e) Weibull plot presenting the 4-point bending strength of conventionally compacted and DIW printed ceramics; (f, f-1) Air bubble and porosity defects observed on fractured surfaces of DIW ceramics.

The microstructure of conventionally compacted and sintered ATZ with 3 wt% alumina platelets (Fig. 4a) showed a random platelet orientation with higher residual porosity than the DIW-processed equivalent (Fig. 4c). As schematically shown in Fig. 4b, nozzle extrusion of DIW efficiently aligned the platelets by the laminar flow of the paste. As the platelet alignment can effectively prevent inter-platelet bridging, a relatively higher density (5.42 $g \cdot cm^{-3}$) was

obtained by DIW than by the conventionally compacted equivalent (5.41 g· cm^{-3}). Importantly, nozzle diameter played a key-role in complete platelet alignment. Above a critical nozzle diameter, the platelets only align in the yield regions near the nozzle wall, whereas the platelets will stay in a random orientation in the nozzle center where the yield stress of the ink exceeds the shear stress [42].

The mechanical properties of the DIW-printed versus conventionally compacted ATZ ceramics were compared in terms of E-modulus, Vickers hardness, toughness and strength (Table 1). The E-modulus and hardness of ATZ ceramics processed by DIW were comparable to that of conventionally compacted ones. The alignment of alumina platelets in DIW-processed 3AP along the printing direction improved the SEVNB fracture toughness (K_{IC}^{V}=7.4 ± 0.3 MPa $m^{0.5}$), when compared to the conventionally compacted 3AP composite (K_{IC}^{V}=6.8 ± 0.3 MPa $m^{0.5}$). Since the two ATZs were processed from the same starting powders under the same sintering conditions, both ATZs presented the same zirconia grain size (0.32±0.01 μm) and zirconia phase transformability (~25 vol% transformed monoclinic zirconia measured on the fracture surfaces of bending bars by XRD). Therefore, the improved fracture toughness for DIW-printed ATZ should be attributed to an enhanced crack-deflection effect of the platelets [57,58]. To confirm this crack-deflection effect of the aligned alumina platelets in DIW-processed ceramics, cracks were induced by Vickers (10 kg) indentation on a polished cross-section of multi-layered materials with changes in the composition (0AP-3AP), as shown in Fig. 4d. The radial cracks were obviously shorter (~55 μm) in the direction perpendicular to than along the platelet planes (~70 μm) in the printed 3AP, which were both shorter than the cracks in the 0AP zone without platelet addition (~75 μm). In comparison, the crack length in conventionally pressed 3AP ceramic (without alignment) was measured to be ~ 63 μm, implying the addition of platelets was beneficial for toughening, regardless of the platelet

orientation. Aligned platelets can provide a stronger but anisotropic toughening effect, explaining the higher SEVNB toughness recorded for the printed 3AP with platelet alignment that revealed much shorter cracks.

The enhanced crack-deflection by platelet alignment also manifested in a higher 4-point bending strength with 1009 ± 93 MPa versus 861 ± 68 MPa for DIW-processed versus conventionally compacted 3AP ceramics. Importantly, the strength ratio between DIW-printed and conventionally compacted ceramics ($\sigma_{average}$-DIW/$\sigma_{average}$-compacted) was the same as their fracture toughness ratio (K_{IC}-DIW/K_{IC}-compacted). Following Griffith's relationship for brittle fracture, the ratio of the critical defect size (*c*) between these two ceramics ($c_{DIW}/c_{compacted}$) was calculated to be ~0.9. This quantitative comparison revealed that the strength improvement of DIW-manufactured ceramics was due to an increased fracture toughness via the aligned platelets. Even more importantly, the processing defects in the hybrid DIW process are similar or even slightly smaller than for the conventional press route. The reliability of DIW processed and conventionally compacted ceramics was similar and the 95% confidence intervals of their Weibull moduli were overlapped showing no statistical difference (Table1). Theoretically, the alignment should also have improved reliability due to the higher toughness, but air bubbles in the DIW-paste still resulted in residual strength-limiting pores, as shown in Fig. 4f, f-1. A spherical pore was found at the fractured surface of the specimen that exhibited the lowest 4-point bending strength, which most likely resulted from air bubbles trapped in the DIW paste. Even though the centrifuge step during DIW-paste preparation (Fig. S1 in the supplementary section) could remove most of the air bubbles in the syringe, a very high rotation speed is needed to remove the smallest air bubbles. However, a too high rotation speed can cause segregation of solid powder from the organic fraction. Therefore, some small air bubbles remained trapped in the paste filament during extrusion,

and resulted in a decreased consistency of the DIW materials [59]. Pores are essentially a discontinuity in the material that can result in thermal stress after sintering or thermal treatment [60]. In addition, the pores might increase the likelihood of local stress concentration around the pore region, while they may lead to crack initiation under an applied external loading and a subsequent reduction in mechanical properties [61,62], especially when the pore is located on the tensile surface of the 4-point bending bar. Noteworthy, the strength of the reference compacted ATZ ceramic is lower than that of state-of-the-art conventionally manufactured ATZs, for which the strength can be significantly higher than 1000 MPa when using granulated powders or for nanocomposites and especially after hot isostatic pressing (HIP) [63,64]. The 2Y-TZP based ATZ used in this work showed a relatively large grain size of 300 nm and a high transformability with the aim of enhancing toughening and reliability. The 25 vol% of transformed *m*-ZrO_2 observed from the fracture surfaces of the bending bars revealed the importance of transformation toughening in the investigated ATZ system. However, the strength has been compromised due to the well-known strength limiting phenomena in transformation-toughened zirconia, i.e., the critical stress to induce the phase transformation[65]. Nevertheless, the transformability of DIW- and compacted ATZs was the same with the same amount of monoclinic zirconia detected on fractured bending specimens. Therefore, hybrid DIW is promising to obtain ceramics with very well controlled processing defects that are similar or even slightly smaller than for the conventional pressing route, but more printable material compositions should be investigated.

Compared to zirconia-based ceramics printed by DIW or SLA [66,67], the proposed hybrid DIW-SLA process provides an easy way to minimize defects and thereby produce dense and crack-free ceramics. The 3Y-TZP and ATZ ceramics previously manufactured by DIW generally had a 4-point or 3-point bending strength up to about 500 MPa, with clearly identified

porosity, cracks and delamination defects [20,66–71]. Crack-free TZPs and ATZ processed by SLA (both laser and DLP) with a strength comparable to those of conventionally fabricated zirconia (~1000 MPa) have been reported in a few studies [72–76], but the printing of multi-layered materials with changes in the composition remains a challenge and the reported strengths spread over a very wide range of ~200-1000 MPa with agglomerates, pores, surface defects and delamination between layers reported as strength-limiting defects[66,67,77]. It is noteworthy that although pores have been observed in some specimens in this work, defects smaller than 10 µm are commonly detected in technical ceramics even for well-established conventional manufacturing processes. The reliability and behavior consistency of the printed and sintered ceramics obtained by this hybrid technique can be further improved by reducing or eliminating the spherical pores that might have originated from small entrapped air bubbles from the paste. Due to the layer-by-layer deposition and weak printing layer interfaces, the strength of AM ceramics is often different in the Z and the XY building directions [78,79]. Further investigation on the anisotropy in mechanical properties and the fatigue behavior of such AM ceramic composites will be conducted. In addition, the hybrid DIW gave rise to a better surface topography as compared to conventional DIW (Fig. S7). Even when using a larger nozzle (250 µm), the surface of the hybrid DIW printed and sintered object was smoother than the ATZ processed by conventional DIW using a hydrogel-based ink (Fig. S7). The improved surface quality obtained by the hybrid approach is in agreement with previous studies [30]. A better shape fidelity has also been reported by using PEG [80] and UV-curing assisted DIW [32]. Therefore, investigations on complex shaped objects with printed and sintered surfaces without polishing should be investigated.

With the improved mechanical performances without post-processing steps, overcoming a main limit of AM ceramics, we believe the approach presented provides a significant

opportunity to fabricate high-performance structural monolithic ceramics with a high level of customization or complex geometrical requirements, such as biomedical implant prostheses, cutting tools with internal cooling channels, high performance valve components, etc. [1]. Although the material choice presented is specific to zirconia composites, there are no reasons why the process could not be applied to other ceramics, such as alumina and non-oxide carbide/nitride/boride-based systems considering also the possibility of using polymer-derived ceramics to make photo-curable paste [81]. In particular, in combination with the opportunities of texturing and multi-material printing, as demonstrated with the printed ceramic laminates with the compositional changes (Fig. 3 and Fig. S6), the principle shown here should also be able to make (textured) ceramic structures with locally tunable mechanical, chemical and electrical properties, like complex shape piezoelectric ceramics [82], interdigitated electrodes for microelectronic devices [83] or functionally graded hip joint components with or without textures [84,85].

3. Conclusion

UV-curing assisted hybrid DIW was successfully applied to fabricate dense and crack-free zirconia-toughened alumina composites with even better mechanical properties than that processed by a conventional pressing. The addition of a non-reactive diluent, like polypropylene glycol, in the photocurable paste is a key-factor in this hybrid AM technology. The addition of a non-reactive water-soluble diluent effectively reduced the polymerization-induced volume shrinkage and the concomitant stresses, allowing to prevent warpage, cracking and delamination during printing and facilitating successful thermal de-binding and sintering. Alumina platelets dispersed in the paste were aligned along the printing direction during nozzle extrusion, enabling a controllable orientation along the building path. The 2Y-

TZP ATZ composite with 3 wt% (4.1 vol%) Al_2O_3 platelets and 17 wt% (23.4 vol%) Al_2O_3 particles had a comparable hardness (13.1 GPa), but better SEVNB fracture toughness (7.4 ± 0.3 MPa $m^{0.5}$) and higher 4-point bending strength (1009 ± 93 MPa) as compared to the conventionally compacted and sintered equivalent. Multi-layered laminate ceramic with compositional changes could be successfully produced without deformation and interfacial defects. The platelet alignment and material composition flexibility of this hybrid UV-curing assisted DIW technology opens up new perspectives for material design and application, since the local composition and concomitant mechanical properties can digitally be integrated into the design of the bulk 3D component.

Table 1. Characteristics of the sintered ATZ ceramics (3AP with 3 wt% alumina platelet).

Ceramic	Packing (vol%)	Relative density (%)	ZrO_2 grain size (µm) [SD]	H_V (GPa)	K_{IC}^V (MPa·$m^{1/2}$), Average [SD]	E-modulus (GPa) [SD]	4-point bending strength (MPa)				
							Average [SD]	Weibull modulus	95% confidence interval of Weibull modulus	Characteristic strength, (MPa)	95% confidence interval of characteristic strength (MPa)
Compacted	53	98.3	0.32 [0.01]	13.3 [0.2]	6.8 [0.3]	256.9 [1.0]	861 [68]	19.7	11.5-28.2	888	823-899
DIW	51	98.4	0.32 [0.01]	13.1 [0.3]	7.4 [0.3]	256.9 [2.0]	1009 [93]	15.1	9.1-20.8	1046	957-1060

4 Experimental Section/Methods

4.1 Materials

Ceramic ATZ comprised 80 wt% 2Y-TZP doped with 0.4 mol% La_2O_3, 17 wt% (23.4 vol%) alumina particles and 3 wt% (4.1 vol%) alumina platelets. 2Y-TZP instead of the widely used 3Y-TZP was used to enhance phase-transformation toughening, whereas the addition of 0.4 mol% lanthanum oxide and alumina particles can effectively improve the resistance to low-temperature degradation (LTD) [36].

The following powders were used to prepare the targeted ATZ powder: 2 mol% yttria-stabilized zirconia (grade TZ-2Y; Tosoh, Tokyo, Japan), α-alumina particles (α-Al_2O_3; Taimicron TM-DAR, Taimei Chemical, Tokyo, Japan), alumina platelets (Alusion, Antaria, Bentley, Australia) and lanthanum nitrate ($La(NO_3)_3 \cdot 6H_2O$, 99 wt%; Chempur, Karlsruhe, Germany). The raw zirconia powder was spray dried with agglomerate size of around 60 µm and a primary crystallite size of 21 nm. The α-alumina particles had a primary particle size of 100 nm with a BET specific surface area of 14.5 m^2/g. The alumina platelets had an average long-axis diameter of ~7.5 µm and thickness of ~200 nm. The zirconia powder was first coated with La_2O_3 by mixing (Turbula type T2C, Basel, Switzerland) lanthanum nitrate and zirconia powder with 5-mm zirconia milling balls (grade TZ-3Y; Tosoh, Tokyo, Japan) in ethanol for 24 h. Then, the suspension was dried in a rotary evaporator at 70°C, followed by drying in an air oven at 90°C for 12 h. The powder was calcined at 750°C for 1 h. The calcined La_2O_3-coated 2Y-TZP powder, α-alumina particles and alumina platelets were mixed and dried again as described above, prior to being sieved with a 315-µm mesh sieve. The ATZ powder mixture was characterized by SEM, as shown in Fig. S1a.

4.2 Paste preparation

Ceramic photocurable paste with a powder load of 51 vol% (84.1 wt%) was composed of the ATZ powder, dispersant, monomers, non-reactive diluent and photoinitiator. The composition of the slurries is summarized in Table S1. The slurries with or without the addition of the non-reactive water-soluble diluent polypropylene glycol (PPEG-400; Sigma Aldrich, Steinheim, Germany), are referred to as 33%PPEG and 0%PPEG, respectively. The ATZ powder and 2.5 wt% (weight to powder) disperbyk-111 (BYK111; BYK additives & instruments, Wesel, Germany) dispersant were firstly mixed using a dual asymmetric centrifugal vacuum mixer (SpeedMixer DAC 400.2 VAC-P, Hauschild, Hamm, Germany) under atmospheric pressure at 2500 rpm for 1 min. Then, two monomers, 1,6 hexanediol diacrylate (HDDA; Sigma Aldrich, Saint Louis, USA) and poly(ethylene glycol) diacrylate-Mn700 (PEGDA; Sigma Aldrich, Tokyo, Japan), and the non-reactive PPEG-400 diluent were mixed with the powder under atmospheric pressure at 2500 rpm for 1 min. Phosphine oxide photoinitiator (TPO; Sigma Aldrich, Saint Louis, USA) with a weight ratio of 0.004 with respect to the monomers was finally added in a dark room. To break the powder agglomerates, 2-mm zirconia milling balls were added to the paste and was mixed under vacuum (150 mbar) at 2500 rpm for 1 min. The slurries were stored in 10-ml UV-light protected syringes. Before printing, the slurry was centrifuged at 5000 rpm for 2 min to remove the potential large air bubbles in the paste/syringe that may have been trapped during the syringe-filling procedure.

4.3 DIW printing, de-binding and sintering

Printing was performed at room temperature (~24°C) in air by a DIW 3D printer (3D Discovery; RegenHU, Villaz-St-Pierre, Switzerland). “Yellow light” was used as room illumination to avoid curing light exposure in the lab. The DIW printer has 4 positions to load syringes with independent pressure control. Objects with a dimension of $4\times3\times30$ mm^3 were printed using conical nozzles (Nordson EFD, Ohio, USA) with a diameter of 250 µm. To avoid voids in-

between adjacent filaments and layers, the line spacing (distance between the axis of two adjacent filaments) and printing layer thickness were both set as 200 μm. As shown in Fig. S1b, subsequent layers were staggered for 100 μm and therefore the new filament was positioned in the groove between two filaments of the previous layer.

Regarding UV-curing, a LED light with a nominal wavelength of 365 nm, 360 mW output power and an irradiance of 8.9 μW/mm² at 200 mm distance was installed in the printer. The air pressure in the syringe was set at 0.25 mbar in combination with a feed rate (moving speed of the nozzle in x-axis) of 10 mm/s. After printing each layer, the extruded paste was UV-cured by scanning the printed object at a speed of 1 mm/s, corresponding to a curing time of 30 s. The UV-curing depth was assessed by measuring the cured thickness of the paste after applying the same polymerization condition as employed during printing. A thin layer of paste was first applied on a glass plate, upon which the glass plate was placed on the building platform and cured at a speed of 1 mm/s. Then, the thickness of the cured layer was measured by removing the uncured paste. The curing depth of 33%PPEG and 0%PPEG was in the range of 410 μm and 280 μm, respectively, which indicated that 250-μm nozzles could be used to print 200-μm thick layers.

After printing, the non-reactive diluent and organic polymer were removed following a two-step procedure, i.e., water de-binding followed by thermal de-binding. Water de-binding was performed by immersing the samples in distilled water for 24 h, followed by drying in an oven at 30°C in air for 24 h. The thermal de-binding process was designed based on prior thermo-gravimetrical analysis and differential scanning calorimetry (TGA/DSC; SDT Q600, TA Instruments, Asse, Belgium). TGA/DSC analysis was conducted on printed 0%PPEG and 33%PPEG (after water de-binding) up to 800°C in air. Accordingly, the water-debinded samples were heated in air at 1°C/min from room temperature to 180°C, followed by a lower

heating rate of 0.5°C/min up to 500°C with a 30-min dwell time. Afterwards, a heating rate of 5°C/min was applied up to 1100°C to pre-sinter the samples for 1 h.

As a reference, the ATZ powder mixture was conventionally shaped by uniaxially pressing at 225 MPa for 40 s (Nannetti Mignon SSN/EA, Nannetti, Italy), followed by cold isostatic pressing (CIP; EPSI, Temse, Belgium) at 300 MPa for 1 min.

All printed and reference materials were pressureless sintered at 1500°C in air for 2 h, with a heating and cooling ramp of 5°C/min.

4.4 Materials characterization

4.4.1 Density and phase analysis

The density of the sintered ceramics was measured according to the Archimedes principle and referred to the theoretical density (TD), calculated by the rule of mixtures. The theoretical density of 2Y-TZP was calculated by the ratio of the molecular weight to the volume of the unit cell to be 5.51 $g \cdot cm^{-3}$, whereas the density of alumina was taken as 3.99 $g \cdot cm^{-3}$ [86].

Phase identification was conducted by X-ray diffraction (XRD; 3003-T/T, Seifert, Ahrensburg, Germany) on polished sintered specimens using Cu-K_α radiation (40 kV and 40 mA) from 20 to 90° 2θ with a step size of 0.02° for 2 s. The amount of *m*-ZrO_2 phase was calculated according to the equation proposed by Garvie *et al*. [87] and modified by Toraya *et al.* [88]. The *t*-ZrO_2 phase transformability was defined as the *t*-*m* ZrO_2 phase transformation on fracture (difference of vol% *m*-ZrO_2 on polished and fracture surfaces of bending bars) and was assessed using XRD in the 27 to 33° 2θ range.

Scanning electron microscopy (SEM, XL-30FEG, FEI, Eindhoven, The Netherlands) was used to characterize the microstructure at 5 kV on mirror-polished and Pt-coated cross-sections.

The microstructure and elemental distributions of Al, La, Zr, O and Y at the interface between 3AP and 0AP were also investigated by electron probe microanalysis (EPMA, JXA-

8530F, JEOL Ltd., Japan), equipped with a wavelength dispersive analysis system and a cold finger trap. The beam current and accelerating voltage were fixed at 100 nA and 15 kV, respectively.

4.4.2 X-ray computed tomography

X-ray computed tomography (XCT; 230 kV/ 300 W TESCAN Unitom XL, TESCAN XRE, Ghent, Belgium) of printed and sintered specimens (without any post-processing including surface polishing) was performed at the KU Leuven XCT Core Facility by mounting the sample on a PSU table and rotating it for 360° around its z-axis. A tungsten target was installed on the reflection source together with a 1-mm thick Sn filter to harden the X-ray beam. 2400 radiographic projections (0.15° rotation step) were acquired, each with an exposure time of 640 ms, while applying a tube voltage of 229 kV and a tube power of 15 W. The number of averages was set to 3 to improve the signal-to-noise ratio, altogether resulting in an acquisition time of 127 min. Cross-sectional image reconstruction, at a voxel size of 2.25 µm, was thereafter performed by applying a filter back-projection algorithm in the TESCAN reconstruction software Panthera.

Further image processing, 3D visualization and quantitative analyses were performed in the Avizo software (v. 2022.2, Thermofisher Scientific). A median filter reduces the noise in dataset further, and the subsequent grey-scale thresholding segments the images into material and pore space. With the thickness map module, the Euclidean distance map in the pore space is calculated and the diameter of the largest inscribed sphere is used as an approximation for the local void size. The output of the thickness map module is used to generate the pore size distribution.

4.4.3. Micro-Raman analysis of polymerization-induced internal stresses

In order to assess curing-induced stresses, micro(μ)-Raman (SENTERRA, BrukerOptik, Ettlingen, Germany) maps were collected at the printed layer interface of cross-sectioned printed and polymerized samples (before de-binding and sintering). An Ar-ion laser source with a wavelength of 532 nm was used through a 20× objective (lateral resolution of ≤ 4 μm). The maps consisted of 60 points in the X-axis and 35 points in the Y-axis with a scanning step size of 4 μm in both axes, resulting in an analysis area of 240×140 μm^2. The Raman wavenumber of the tetragonal zirconia band at around 147 cm^{-1} was used to analyze the residual stress state by fitting the Raman spectra with a Lorentzian function using curve-fitting software (Fityk 1.2.1, Marcin Wojdyr, Poland). A peak shift towards lower wavenumbers indicates the presence of tensile stress, whereas a peak shift towards a higher wavenumber implies the presence of compressive stress. The statistical R software package (R3.6.2, R foundation for statistical computing, Vienna, Austria) was used to compute the μ-Raman data and draw the filled contour plots.

4.4.4 Mechanical characterization of sintered ceramics

An indentation tester (Model FV-700, Future-Tech, Tokyo, Japan) was used to measure the Vickers hardness (H_V) on mirror-polished surfaces with a load of 98.1 N for 10 s. Ten measurements were performed on each sample.

Single-Edge-V-Notched Beam (SEVNB) specimens were used to study the effect of alumina platelet alignment on the fracture toughness (K_{IC}^V). Bars (n=5/grade) of 25×3×2 mm^3 were prepared according to previous literature reports and ISO 6872:2015 [89,90]. A notch was prepared by a razor blade with 3 μm and 1 μm diamond paste. For AM-prepared specimens, the notch was cut in the direction perpendicular to the filament axis, while no preferential orientation was chosen in conventionally compacted reference samples. After notch preparation, all SEVNB specimens were annealed in air at 1200°C for 30 min for stress

annealing. The specimens were loaded into a four-point bending (4PB) setup with an outer and inner span of 20 and 10 mm, respectively, at a crosshead speed of 0.5 mm/min using a hydraulic testing machine (Instron 4467, Instron, Norwood, MA, USA).

The Young's modulus (*E*) of the AM-prepared and compacted materials was comparatively measured by the Impulse Excitation Technique (IET) (GrindoSonic MK7, Leuven, Belgium) (n=2/grade, 10 times for each sample) on 4PB samples, according to ASTM E1876-99.

The flexural strength was assessed by 4PB testing using 25×3×2-mm^3 bars (n=15/grade) prepared according to ISO 6872:2015 [90]. The surface subjected to tensile stress was mirror-polished. The 4PB-strength results were analyzed by Weibull statistics to determine the characteristic strength and the Weibull modulus applying the Maximum-Likelihood-estimation with confidence bounds ($\alpha = 0.05$). The specimens were fractured following the same set-up as used for the SEVNB fracture-toughness test with a crosshead speed of 0.5 mm/min.

Acknowledgements

Maoyin Li thanks the China Scholarship Council (CSC No. 201806460096) for financial support. This research was supported by the Research Fund of KU Leuven project C2-17-00402, and the Fund for Scientific Research - Flanders (FWO Vlaanderen) (grant number G.0431.10N and G.0959.20N). F. Zhang thanks the Scientific Research - Flanders (FWO-Vlaanderen) for her post-doctoral fellowships (grant numbers 12S8418N & 12S8421N). The authors would also like to acknowledge the KU Leuven, project C24/17/052. The KU Leuven XCT Core facility is acknowledged for the 3D image acquisition and post-processing tools (https://xct.kuleuven.be/). We thank Berfu Göksel for providing the reference ATZ sample

that was processed by conventional DIW for surface topography investigations, and we thank Berfu Göksel and Mrinal Srivastava for assisting the surface topography measurements.

CRediT author statement

Maoyin Li (Conceptualization: Supporting; Data curation: Lead; Formal analysis: Lead; Investigation: Lead; Methodology: Lead; Writing – original draft: Lead; Writing – review & editing: Supporting)

Shuigen Huang (Investigation: Supporting; Data Curation: supporting; Formal analysis: supporting; Methodology: Supporting; Writing – review & editing: Supporting)

Evita Willems (Methodology: Supporting; Writing – review & editing: Supporting)

Jeroen Soete (Methodology: Supporting; Writing – review & editing: Supporting)

Masanao Inokoshi (Methodology: Supporting)

Bart Van Meerbeek (Funding acquisition: Supporting; Supervision: Supporting; Writing – review & editing: Supporting)

Jef Vleugels (Funding acquisition: Lead; Supervision: lead; Writing – review & editing: Supporting)

Fei Zhang (Conceptualization: Lead; Formal analysis: Supporting; Funding acquisition: Lead; Investigation: Supporting; Methodology: Lead; Project administration: Lead; Supervision: Lead; Writing – review & editing: Lead)

Supplementary documents

Supplementary experimental section/methods

The surface topography of printed and sintered ceramics was evaluated using a 3D optical non-contact profilometer (S neox, Sensofar, Barcelona, Spain). The topography was acquired using a confocal objective of 50x magnification with a scanning step of 1 µm. Two sample grades were evaluated: 33%PPEG printed by UV-curing assisted DIW and a comparative ATZ printed by conventional DIW. The printable paste for conventional DIW printing was based on 25 wt% thermosensitive Pluronic F-127 hydrogel and 42 vol% ATZ was loaded. The extrusion for conventional DIW was performed through a conical nozzle with a diameter of 200 µm, and the comparative ATZ was pressureless sintered at 1500°C for 2 hours. After the surface topography acquisition, the surface was leveled to ensure a flat baseline and the waviness of the surface was not filtered, as the waviness is the topography that needs to be studied.

Supplementary results

Table S1. Paste composition with 51 vol% ATZ solid loading. HDDA, PEGDA and PPEG-400 were added in a 7:3:0 or 1:1:1 vol% ratio, being referred to 0%PPEG and 33%PPEG, respectively. The weight percentage of the paste compounds are shown in the table.

Paste	ATZ	BYK111	HDDA	PEGDA	PPEG-400	TPO
	Powder	Dispersant	Monomers		Non-reactive diluent	Photoinitiator
0%PPEG	84.089	2.102	9.323	4.431	-	0.055
33%PPEG	84.083	2.102	4.432	4.914	4.432	0.037

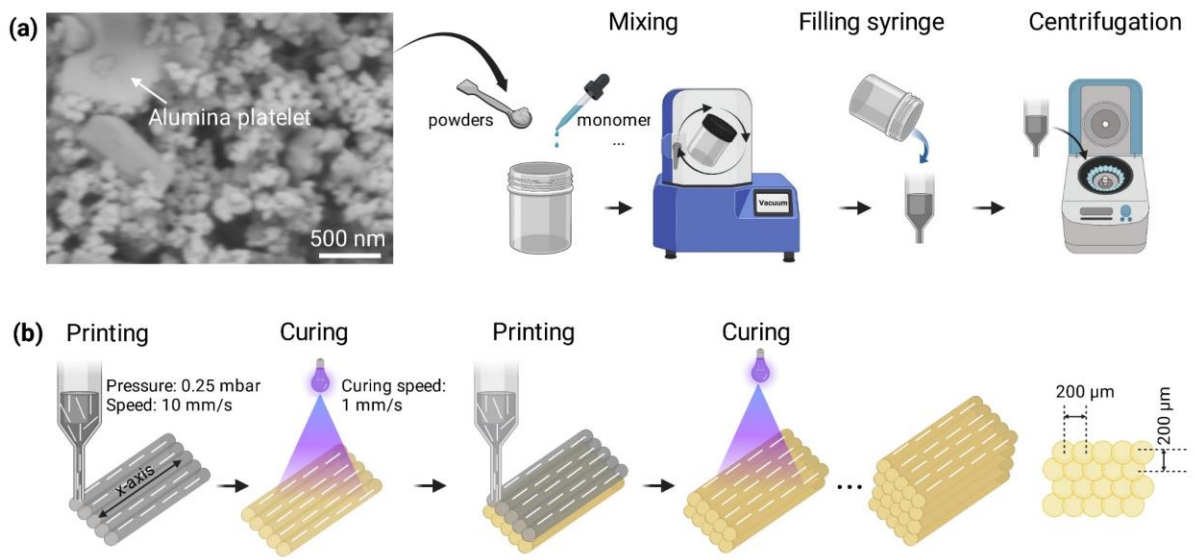

Fig. S1. Paste preparation and DIW printing process: (a) SEM image of the ATZ powder and the paste-preparation process, and (b) the printing process consisting of DIW-filament extrusion and subsequent curing.

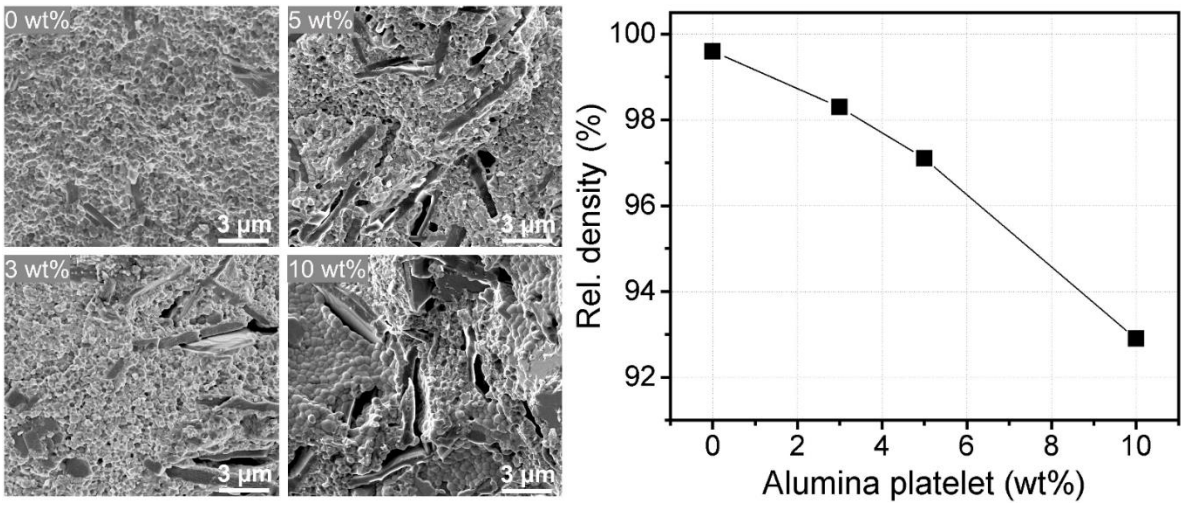

Fig. S2. Inter-platelet bridging caused porosities and decreased density with increased alumina platelet addition.

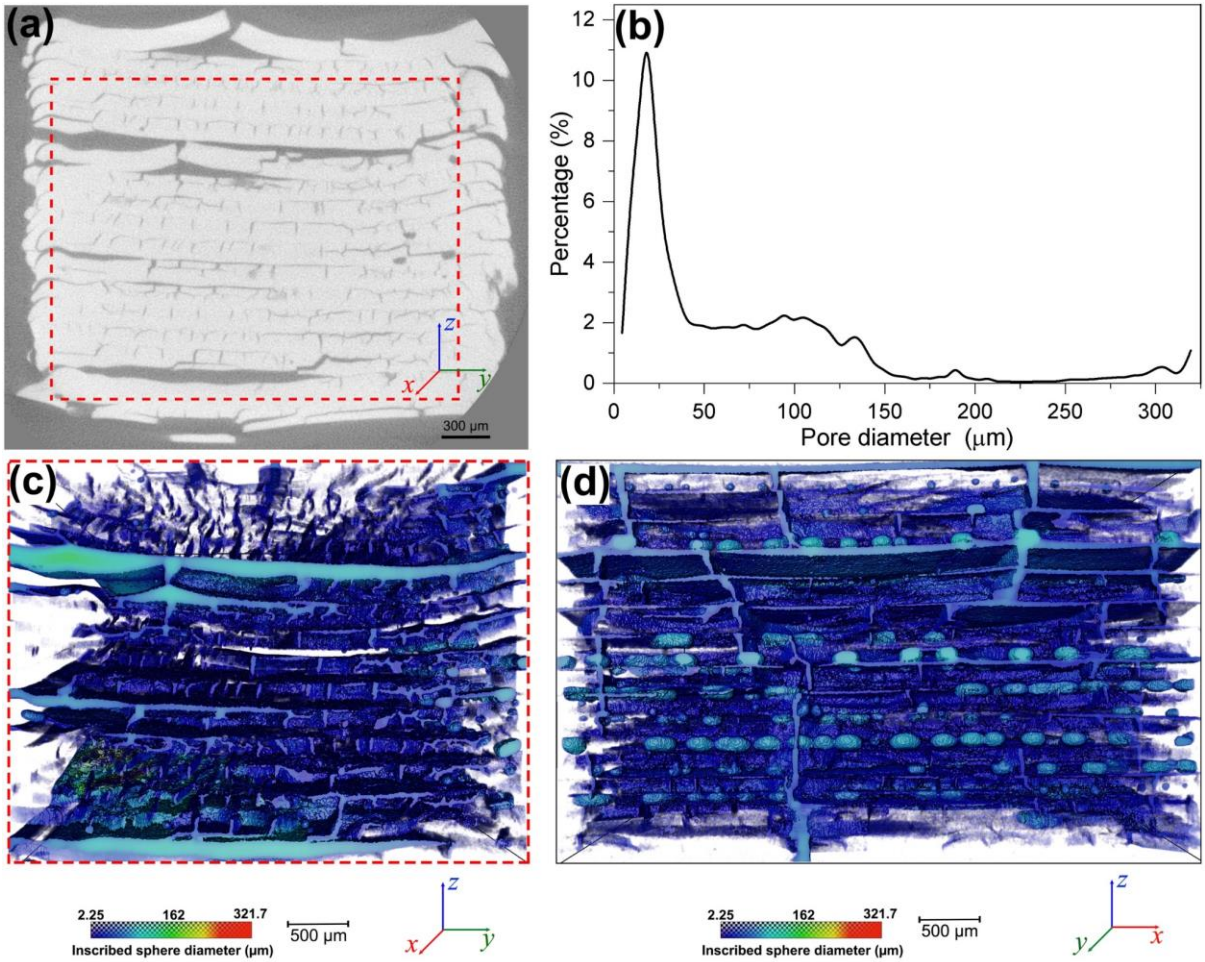

Fig. S3. XCT analysis of sintered 0%PPEG (51 vol% powder-loading based slurry): (a) representative XCT slice, (b) size distribution of the defects detected by XCT and (c, d) the 3D-reconstruction of the defects.

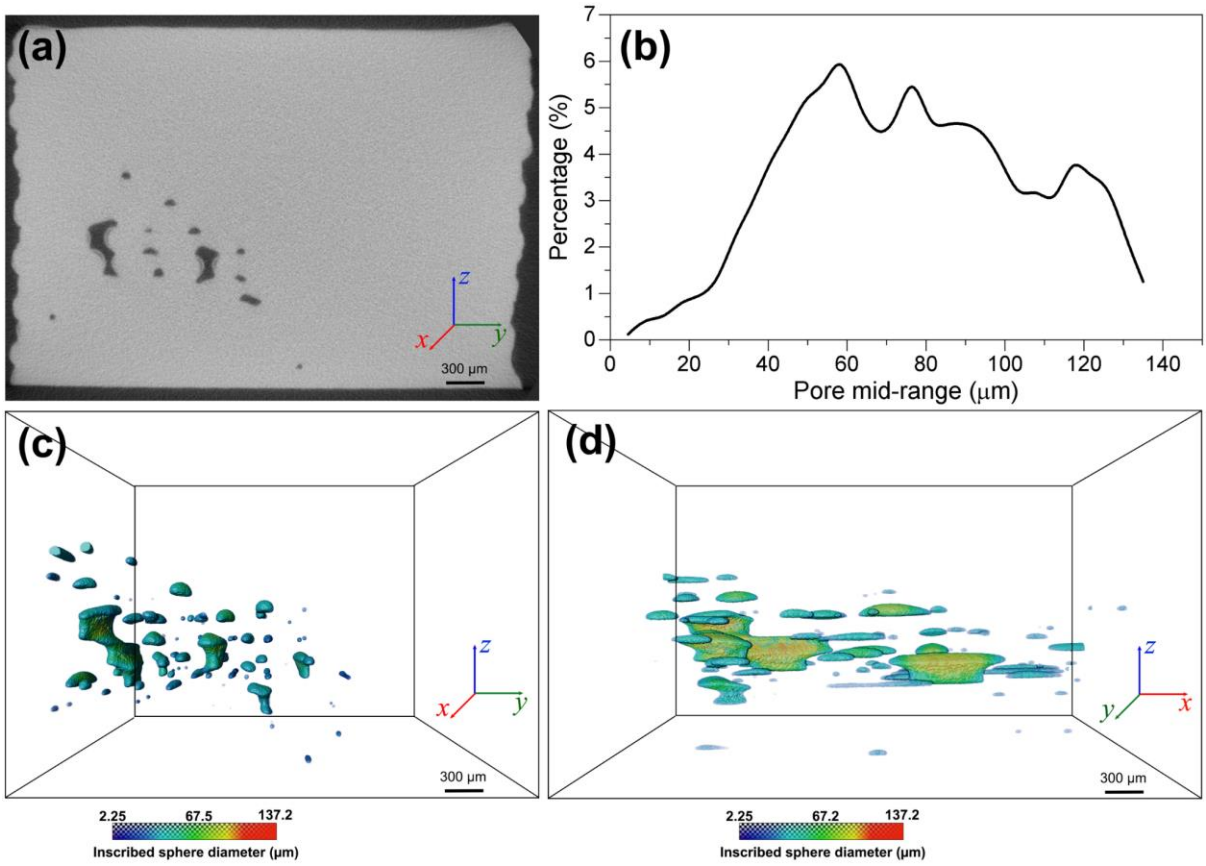

Fig. S4. XCT analysis of sintered 33%PPEG from 53 vol% powder-loading based slurry: (a) representative XCT slice, (b) size distribution of the defects detected by XCT and (c, d) 3D-reconstruction of the triangle-shaped defects in-between the filaments.

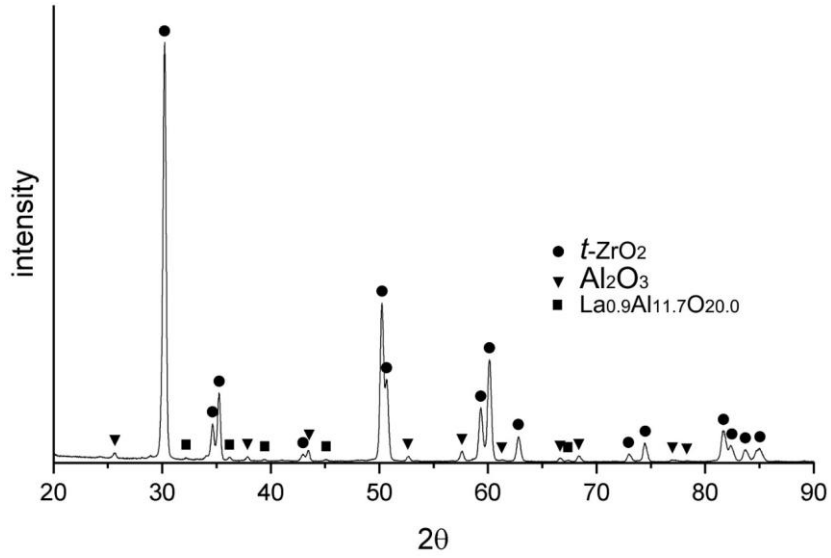

Fig. S5. XRD patterns of a polished printed and sintered ATZ (33%PPEG).

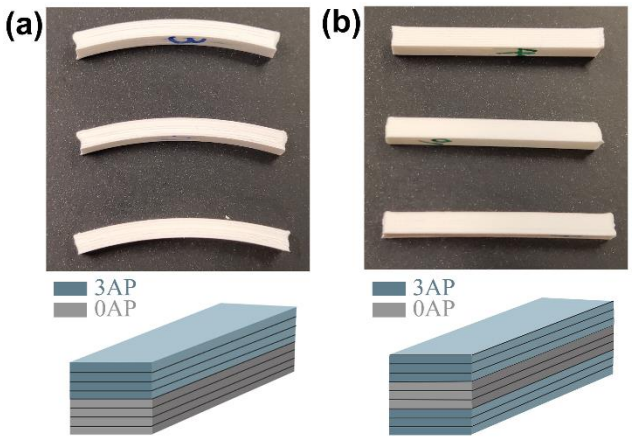

Fig. S6. (a) Asymmetric laminate specimen composed of 3AP and 0AP. (b) Sandwich configuration with 0AP core layers surrounded by 3AP layers.

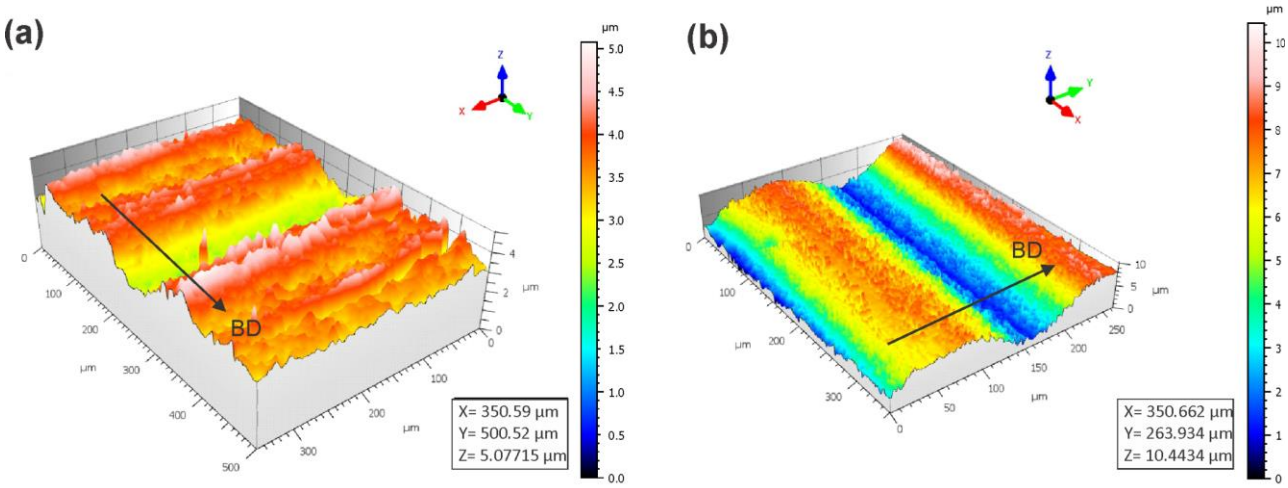

Fig. S7. Surface topography of DIW-printed and sintered ATZs: (a) ATZ printed by UV-curing assisted DIW (33%PPEG) using a 250 µm nozzle, as described in the main manuscript and (b) comparative ATZ printed by conventional DIW using a hydrogel-based ink and 200 µm nozzle. BD is the building direction.

Reference

[1] Y. Lakhdar, C. Tuck, J. Binner, A. Terry, R. Goodridge, *Prog. Mater. Sci.* **2020**, *116*, 100736.

[2] G. Ding, R. He, K. Zhang, C. Xie, M. Wang, Y. Yang, D. Fang, *J. Am. Ceram. Soc.* **2019**, *102*, 7198.

[3] E. Peng, D. Zhang, J. Ding, *Adv. Mater.* **2018**, *30*, 1802404.

[4] J. W. Kemp, A. A. Diaz, E. C. Malek, B. P. Croom, Z. D. Apostolov, S. R. Kalidindi, B. G. Compton, L. M. Rueschhoff, *Addit. Manuf.* **2021**, *44*, 102049.

[5] J. A. Lewis, G. M. Gratson, *Mater. Today* **2004**, *7*, 32.

[6] L. Rueschhoff, W. Costakis, M. Michie, J. Youngblood, R. Trice, *Int. J. Appl. Ceram. Technol.* **2016**, *13*, 821.

[7] W. J. Costakis, L. M. Rueschhoff, A. I. Diaz-Cano, J. P. Youngblood, R. W. Trice, *J. Eur. Ceram. Soc.* **2016**, *36*, 3249.

[8] E. Feilden, E. G. T. Blanca, F. Giuliani, E. Saiz, L. Vandeperre, *J. Eur. Ceram. Soc.* **2016**, *36*, 2525.

[9] B. Utela, D. Storti, R. Anderson, M. Ganter, *J. Manuf. Process.* **2008**, *10*, 96.

[10] N. Reis, C. Ainsley, B. Derby, *J. Am. Ceram. Soc.* **2005**, *88*, 802.

[11] Z. Rahman, S. F. Barakh Ali, T. Ozkan, N. A. Charoo, I. K. Reddy, M. A. Khan, *AAPS J.* **2018**, *20*, 1.

[12] F. Zhang, B. C. Spies, E. Willems, M. Inokoshi, C. Wesemann, S. M. Cokic, B. Hache, R. J. Kohal, B. Altmann, J. Vleugels, B. Van Meerbeek, K. Rabel, *Acta Biomater.* **2022**, *150*, 427.

[13] R. Galante, C. G. Figueiredo-Pina, A. P. Serro, *Dent. Mater.* **2019**, *35*, 825.

[14] S. Y. Song, M. S. Park, D. Lee, J. W. Lee, J. S. Yun, *Mater. Des.* **2019**, *180*, 107960.

[15] S. Zakeri, M. Vippola, E. Levänen, *Addit. Manuf.* **2020**, *35*, 101177.

[16] Q. Cai, S. Meille, J. Chevalier, S. Zhou, F. Bouville, I. Tirichenko, E. Saiz, *Mater. Des.* **2023**, *225*, 111463.

[17] S. Lamnini, H. Elsayed, Y. Lakhdar, F. Baino, F. Smeacetto, E. Bernardo, *Heliyon* **2022**, *8*, 10651.

[18] D. Zhang, W. Jonhson, T. S. Herng, Y. Q. Ang, L. Yang, S. C. Tan, E. Peng, H. He, J. Ding, *Mater. Horizons* **2020**, *7*, 1083.

[19] J. M. Mccracken, A. Badea, M. E. Kandel, A. S. Gladman, D. J. Wetzel, G. Popescu, J. A. Lewis, R. G. Nuzzo, *Adv. Healthc. Mater.* **2016**, *5*, 1025.

[20] E. Peng, X. Wei, U. Garbe, D. Yu, B. Edouard, A. Liu, J. Ding, *J. Mater. Sci.* **2018**, *53*, 247.

[21] X. Xu, J. Yang, W. Jonhson, Y. Wang, A. Suwardi, J. Ding, C. Guan, D. Zhang, *Addit. Manuf.* **2022**, *56*, 102939.

[22] J. Zhang, M. Yarahmadi, L. Cabezas, M. Serra, S. Elizalde, J. M. Cabrera, L. Llanes, G. Fargas, *J. Eur. Ceram. Soc.* **2023**, *43*, 2794.

[23] J. Chevalier, A. Liens, H. Reveron, F. Zhang, P. Reynaud, T. Douillard, L. Preiss, V. Sergo, V. Lughi, M. Swain, N. Courtois, *J. Am. Ceram. Soc.* **2020**, *103*, 1482.

[24] N. Travitzky, A. Bonet, B. Dermeik, T. Fey, I. Filbert-Demut, L. Schlier, T. Schlordt, P. Greil, *Adv. Eng. Mater.* **2014**, *16*, 729.

[25] A. M'Barki, L. Bocquet, A. Stevenson, *Sci. Rep.* **2017**, *7*, 1.

[26] M. Faes, J. Vleugels, F. Vogeler, E. Ferraris, *CIRP J. Manuf. Sci. Technol.* **2016**, *14*, 28.

[27] X. He, J. Xu, W. Ji, *J. Sol-Gel Sci. Technol.* **2022**, *104*, 276.

[28] D. Zhang, E. Peng, R. Borayek, J. Ding, *Adv. Funct. Mater.* **2019**, *29*, 1.

[29] L. Wei, J. Li, S. Zhang, B. Li, Y. Liu, F. Wang, S. Dong, *Ceram. Int.* **2020**, *46*, 3637.

[30] H. Wang, C. Chen, F. Yang, Y. Shao, Z. Guo, *Mater. Today Commun.* **2021**, *26*, 102037.

[31] J. W. Jeon, W. Y. Maeng, H. Lee, Y. H. Koh, H. E. Kim, *J. Eur. Ceram. Soc.* **2021**, *41*, 6729.

[32] D. A. Rau, J. S. Bryant, J. P. Reynolds, M. J. Bortner, C. B. Williams, *Addit. Manuf.* **2023**, *72*, 103616.

[33] S. Cailliet, M. Roumanie, C. Croutxé-Barghorn, G. Bernard-Granger, R. Laucournet, *Ceram. Int.* **2021**, *47*, 3892.

[34] A. Zocca, P. Colombo, C. M. Gomes, J. Günster, *J. Am. Ceram. Soc.* **2015**, *98*, 1983.

[35] T. Campbell, C. Williams, O. Ivanova, B. Garrett, in *Atl. Counc.*, Atlantic Council, Washington, **2011**.

[36] F. Zhang, J. Chevalier, C. Olagnon, B. Van Meerbeek, J. Vleugels, *J. Eur. Ceram. Soc.* **2017**, *37*, 1865.

[37] F. Bouville, E. Maire, S. Meille, B. Van De Moortèle, A. J. Stevenson, S. Deville, *Nat. Mater.* **2014**, *13*, 508.

[38] M. Kotoul, J. Pokluda, P. Šandera, I. Dlouhý, Z. Chlup, A. R. Boccaccini, *Acta Mater.* **2008**, *56*, 2908.

[39] M. Li, B. Van Meerbeek, B. Tunca, S. Cokic, J. Vleugels, F. Zhang, *J. Eur. Ceram. Soc.* **2021**, *41*, 247.

[40] P. Maillard, J. E. Aubert, *Constr. Build. Mater.* **2014**, *63*, 56.

[41] Y. Sanomura, M. Kawamura, *Polym. Compos.* **2003**, *24*, 587.

[42] B. G. Compton, J. A. Lewis, *Adv. Mater.* **2014**, *26*, 5930.

[43] W. Huang, D. Restrepo, J. Y. Jung, F. Y. Su, Z. Liu, R. O. Ritchie, J. McKittrick, P. Zavattieri, D. Kisailus, *Adv. Mater.* **2019**, *31*, 1901561.

[44] E. Feilden, C. Ferraro, Q. Zhang, E. García-Tuñón, E. D'Elia, F. Giuliani, L. Vandeperre, E. Saiz, *Sci. Rep.* **2017**, *7*, 13759.

[45] N. Kleger, S. Fehlmann, S. S. Lee, C. Dénéréaz, M. Cihova, N. Paunović, Y. Bao, J. Leroux, S. J. Ferguson, K. Masania, A. R. Studart, *Adv. Mater.* **2022**, *34*, 2203878.

[46] M. R. Bouschlicher, M. A. Vargas, D. B. Boyer, *Am. J. Dent.* **1997**, *10*, 88.

[47] E. Johansson, O. Lidström, J. Johansson, O. Lyckfeldt, E. Adolfsson, *Materials (Basel).* **2017**, *10*, 138.

[48] Y. Jian, Y. He, T. Jiang, C. Li, W. Yang, J. Nie, *J. Coatings Technol. Res.* **2013**, *10*, 231.

[49] C. Qian, K. Hu, Z. Lu, P. Li, *Mater. Chem. Phys.* **2021**, *267*, 124661.

[50] C. Qian, K. Hu, J. Li, P. Li, Z. Lu, *J. Eur. Ceram. Soc.* **2021**, *41*, 7141.

[51] S. Zakeri, M. Vippola, E. Levänen, *Addit. Manuf.* **2020**, *35*, 101177.

[52] A. Peutzfeldt, *Eur. J. Oral Sci.* **1997**, *105*, 97.

[53] M. Goldman, *Aust. Dent. J.* **1983**, *28*, 156.

[54] K. Mequanint, R. D. Sanderson, *Macromol. Symp.* **2003**, *193*, 169.

[55] J. Kim, C. W. Gal, Y.-J. Choi, H. Park, S.-Y. Yoon, H. Yun, *Addit. Manuf.* **2023**, *67*, 103475.

[56] K. Wang, M. Qiu, C. Jiao, J. Gu, D. Xie, C. Wang, X. Tang, Z. Wei, L. Shen, *Ceram. Int.* **2020**, *46*, 2438.

[57] K. T. Faber, A. G. Evans, *Acta Metall.* **1983**, *31*, 565.

[58] X. -N Huang, P. S. Nicholson, *J. Am. Ceram. Soc.* **1993**, *76*, 1294.

[59] C. Liu, J. Gao, Y. Tang, X. Chen, *J. Mater. Sci.* **2018**, *53*, 16415.

[60] U. Lohbauer, G. Amberger, G. D. Quinn, S. S. Scherrer, *J. Mech. Behav. Biomed. Mater.* **2010**, *3*, 623.

[61] Z. Li, Y. Jing, H. Guo, X. Sun, K. Yu, A. Yu, X. Jiang, X. J. Yang, *Metall. Mater. Trans. B Process Metall. Mater. Process. Sci.* **2019**, *50*, 1204.

[62] T. Zhou, C. Huang, *Comput. Mater. Sci.* **2015**, *104*, 177.

[63] P. Palmero, L. Montanaro, H. Reveron, J. Chevalier, *Materials (Basel).* **2014**, *7*, 5012.

[64] P. Palmero, *Nanomaterials* **2015**, *5*, 656.

[65] M. V. SWAIN, L. R. F. ROSE, *J. Am. Ceram. Soc.* **1986**, *69*, 511.

[66] M. Saâdaoui, F. Khaldoun, J. Adrien, H. Reveron, J. Chevalier, *J. Eur. Ceram. Soc.* **2020**, *40*, 3200.

[67] E. Willems, M. Turon-Vinas, B. Camargo dos Santos, B. Van Hooreweder, F. Zhang, B. Van Meerbeek, J. Vleugels, *J. Eur. Ceram. Soc.* **2021**, *41*, 5292.

[68] H. Shao, D. Zhao, T. Lin, J. He, J. Wu, *Ceram. Int.* **2017**, *43*, 13938.

[69] W. Li, A. Ghazanfari, D. McMillen, M. C. Leu, G. E. Hilmas, J. Watts, *Ceram. Int.* **2018**, *44*, 12245.

[70] Y. Shi, W. Wang, *Mater. Lett.* **2020**, *261*, 127131.

[71] T. Yu, Z. Zhang, Q. Liu, R. Kuliiev, N. Orlovskaya, D. Wu, *Ceram. Int.* **2020**, *46*, 5020.

[72] J. Sun, X. Chen, J. Wade-Zhu, J. Binner, J. Bai, *Addit. Manuf.* **2021**, *43*, 101994.

[73] H. Nakai, M. Inokoshi, K. Nozaki, K. Komatsu, S. Kamijo, H. Liu, M. Shimizubata, S. Minakuchi, B. Van Meerbeek, J. Vleugels, F. Zhang, *Materials (Basel).* **2021**, *14*, 3694.

[74] Y. Lu, Z. Mei, J. Zhang, S. Gao, X. Yang, B. Dong, L. Yue, H. Yu, *J. Eur. Ceram. Soc.* **2020**, *40*, 826.

[75] X. Fu, B. Zou, H. Xing, L. Li, Y. Li, X. Wang, *Ceram. Int.* **2019**, *45*, 17630.

[76] A. Zenthöfer, F. S. Schwindling, C. Schmitt, A. Ilani, N. Zehender, P. Rammelsberg, S. Rues, *Dent. Mater.* **2022**, *38*, 1565.

[77] K. J. Jang, J. H. Kang, J. G. Fisher, S. W. Park, *Dent. Mater.* **2019**, *35*, e97.

[78] C. Marsico, M. Øilo, J. Kutsch, M. Kauf, D. Arola, *Addit. Manuf.* **2020**, *36*, 101450.

[79] B. Coppola, J. Schmitt, T. Lacondemine, C. Tardivat, L. Montanaro, P. Palmero, *J. Eur. Ceram. Soc.* **2022**, *42*, 2974.

[80] M. Maillard, J. Chevalier, L. Gremillard, G. P. Baeza, E.-J. Courtial, S. Marion, V. Garnier, *J. Eur. Ceram. Soc.* **2023**, *43*, 2805.

[81] Z. C. Eckel, C. Zhou, J. H. Martin, A. J. Jacobsen, W. B. Carter, T. A. Schaedler, *Science (80-.).* **2016**, *351*, 58.

[82] Y. Li, L. Li, B. Li, *Materials (Basel).* **2015**, *8*, 1729.

[83] K. Fu, Y. Wang, C. Yan, Y. Yao, Y. Chen, J. Dai, S. Lacey, Y. Wang, J. Wan, T. Li, Z. Wang, Y. Xu, L. Hu, *Adv. Mater.* **2016**, *28*, 2587.

[84] S. Rouf, A. Malik, A. Raina, M. Irfan, U. Haq, N. Naveed, A. Zolfagharian, M. Bodaghi, *J. Orthop.* **2022**, *33*, 70.

[85] R. L. Walton, E. R. Kupp, G. L. Messing, L. Livermore, *J. Mater. Res.* **2021**, *36*, 3591.

[86] I. Levin, D. Brandon, *J. Am. Ceram. Soc.* **1998**, *81*, 1995.

[87] R. C. Garvie, P. S. Nicholson, *J. Am. Ceram. Soc.* **1972**, *55*, 303.

[88] H. Toraya, M. Yoshimura, S. Somiya, *J. Am. Ceram. Soc.* **1984**, *67*, 119.

[89] J. Kübler, in *Ceram. Eng. Sci. Proc.*, **1997**, pp. 155–162.

[90] *ISO 6872: 2015. Dentistry — Ceramic Materials*, **2015**.